# Next-generation in vivo optical imaging with short-wave infrared quantum dots

# Next generation *in vivo* optical imaging with short-wave infrared quantum dots

Oliver T. Bruns[1#]*, Thomas S. Bischof[1#]*, Daniel K. Harris[1,2], Yanxiang Shi[3], Lars Riedemann[4], Alexander Bartelt[5], Frank B. Jaworski[6], Daniel Franke[1], Jessica A Carr[1], Christopher J. Rowlands[7], Mark WB Wilson[1], Ou Chen[1], He Wei[1], Gyu Weon Hwang[1,2,8], Daniel Montana[1,2], Igor Coropceanu[1], Jonas Kloepper[4], Joerg Heeren[9], Peter T.C. So[7,10], Dai Fukumura[4], Klavs F. Jensen[3], Rakesh K. Jain[4] and Moungi G. Bawendi[1]*

[1] Department of Chemistry, Massachusetts Institute of Technology, 77 Massachusetts Ave., Cambridge, MA 02139 (USA)

[2] Department of Materials Science and Engineering, Massachusetts Institute of Technology, 77 Massachusetts Ave., Cambridge, MA 02139 (USA)

[3] Department of Chemical Engineering, Massachusetts Institute of Technology, 77 Massachusetts Ave., Cambridge, MA 02139 (USA)

4 Edwin L. Steele Lab for Tumor Biology, Massachusetts General Hospital and Harvard Medical School, 100 Blossom St., Boston, MA 02114 (USA)

[5] Department of Genetics and Complex Diseases and Sabri Ülker Center, Harvard T.H. Chan School of Public Health, 665 Huntington Ave., Boston, MA 02115 (USA)

[6] Raytheon Vision Systems, Goleta, California 93117 (USA)

[7] Department of Biological Engineering, Massachusetts Institute of Technology, Cambridge, Massachusetts (USA)

[8] now at Korea Institute of Science and Technology, Seoul, 02792, (Republic of Korea)

[9] Department of Biochemistry and Molecular Cell Biology, University Medical Center Hamburg-Eppendorf, Martinistrasse 52, 20246 Hamburg, Germany

[10] Department of Mechanical Engineering, Massachusetts Institute of Technology, Cambridge, Massachusetts (USA)

#Both authors contributed equally

*Correspondence to: obruns@mit.edu, tbischof@mit.edu and mgb@mit.edu

## Abstract

The short-wavelength infrared region (SWIR; 1000—2000 nm) provides several advantages over the visible and near-infrared regions for *in vivo* imaging. The general lack of autofluorescence, low light absorption by blood and tissue, and reduced scattering can render a mouse translucent when imaged in the SWIR region. Despite these advantages, the lack of a versatile emitter platform has prevented its general adoption by the biomedical research community. Here we introduce high-quality SWIR-emitting core/shell quantum dots (QDs) for the next generation of *in vivo* SWIR imaging. Our QDs exhibit a dramatically higher emission quantum yield (QY) than previously described SWIR probes, as well as a narrow and size-tunable emission that allows for multiplexing in the SWIR region. To demonstrate some of its capabilities, we used this imaging platform to measure the heartbeat and breathing rates in awake and unrestrained mice, as well as to quantify the metabolic turnover rates of lipoproteins in several organs simultaneously in real time in mice. Finally, we generate detailed three-dimensional quantitative flow maps of brain vasculature by intravital microscopy and visualize the differences between healthy tissue and a tumor in the brain. In conclusion, SWIR QDs enable biological optical imaging with an unprecedented combination of deep penetration, high spatial resolution, and fast acquisition speed.

## Introduction

In order to understand the molecular and cellular mechanisms involved in physiology and disease, biomedical research increasingly aims toward non-invasive imaging with cellular resolution *in vivo*. Fluorescent probes in particular can be detected with very high sensitivity, ultimately allowing the resolution and tracking of single labeled biological entities. This enables the study of rapid biological processes in greater detail than other imaging modalities, such as magnetic resonance imaging (MRI), ultrasound (US) or computed tomography (CT). However, when imaging whole organisms several biological obstacles remain which reduce the sensitivity, acquisition speed, and spatial resolution of fluorescence imaging. Autofluorescence of tissues or cells add a background signal, decreasing the contrast and therefore the sensitivity; absorption and scattering of the excitation and emission light by blood and other tissue limits signal detection and impacts acquisition speeds; and scattering limits the spatial resolution as a function of depth, causing blurring of the acquired image.

Imaging in the short-wavelength infrared (SWIR; 1000—2000 nm) region addresses all of these challenges simultaneously. The minimal autofluorescence of biological tissue in the SWIR region leads to increased sensitivity[1,2], while the significantly reduced light attenuation from scattering and from absorption from blood and other structures enables imaging with high spatiotemporal resolution and penetration depth[2–8]. Consequently, large organisms like a whole mouse may be rendered translucent when imaged using SWIR fluorescence[3,7,9].

Thus far, the lack of a versatile SWIR emitter technology has prevented the general adoption of SWIR *in vivo* imaging despite its advantages over visible and near-IR imaging. Versatile probes ideally need to combine a high fluorescence quantum yield (QY) for sensitive and fast imaging, a tunable and narrow emission to generate different colors for multiplexing, and appropriate functionalization for specific biological applications.

Here we introduce SWIR-emitting InAs-based quantum dots (QDs) as versatile probes for biological imaging. These QDs exhibit a dramatically higher QY and stability than previously described SWIR probes[1,2,7,8,10–16], as well as a narrow and size-tunable emission spectrum comparable to established visible-light emitting QDs[17]. To demonstrate some of the capabilities of this imaging platform, we use color-multiplexed imaging to simultaneously detect perfusion and uptake of functionalized QDs in the same mouse. We directly quantify metabolic processes in real time using QD-labelled lipoproteins, by non-invasively imaging their transition between brown adipose tissue (BAT), blood and liver. We use long-circulating PEGylated QDs to assess and quantify heartrate and respiration of both sedated and awake mice. We perform angiography in the brain of a mouse, directly identifying arteries and veins. We use QD composite particles to visualize the dramatic differences between flow of blood in healthy vasculature and in vessels at the tumor margin. We finally exploit our ability to track individual QD composite particles to quantify blood flow in the vasculature of the brain, with sufficient spatial resolution to measure flow in individual capillaries.

# Results

## Characterization of the core/shell QDs

The emission of core/shell QDs in the SWIR band is size-tunable, with the InAs/CdSe/ZnSe QDs (figure 1a) in this work covering the 1050—1400 nm spectral range. Our InAs/CdSe and InAs/CdSe/ZnSe QDs (supplementary figures 1 and 2) typically had QYs of 10—20% in physiological saline solution, stable over several months (supplementary figure 3), and our best sample had a QY of 30%. These QYs are more than one hundred times higher than those of

carbon nanotubes (CNTs; 0.1%) and roughly ten times higher than the best performing SWIR emitting materials previously applied to biological imaging[7,8,10,12–16,18] (figure 1b).[A]

Tunable emission allows for the generation of multiple colors in the SWIR band (figure 1c and 1d, and supplementary video 1). There is little change in the emission spectra and the QYs remain high after transfer of the QDs from the organic phase, they were synthesized in, into buffer, achieved here by incorporating the QDs into PEG2000-phospholipids micelles (figure 1e)[19,20].

In addition to high QY, short photoluminescence lifetimes are important for high-flux applications such as confocal microscopy, because the lifetime sets both the maximum excitation flux before saturation is reached and the limit on overall emission output. For our samples of InAs QDs, we measured photoluminescence lifetimes on the order of 100 ns (supplementary figures 4 and 5), which is about one order of magnitude faster than comparable Pb-based QDs..

## Color SWIR imaging

The size-tunable emission was used for spectral SWIR imaging *in vivo*, generating a two-color SWIR image of a nude mouse injected with QDs through different administration routes, e.g. intraperitoneal (i.p.) application of “green” SWIR QDs and intravenous (i.v.) application of “red” SWIR QDs (figure 1f). The i.p. injected “green” SWIR QDs showed a signal pattern consistent with a distribution throughout the peritoneal cavity, while the i.v. injected “red” SWIR QDs labelled all tissues.

The emission spectra were narrow and distinct enough to be separated by the use of edge-pass filters (figure 2a), without the need for linear unmixing. *In vivo*, we used differently functionalized

[A] We used an integrating sphere for our QY measurements and our measured QY for CNTs is lower than that found in previous reports, which used the dye IR-26 as a QY reference. These earlier values rely on a reported QY for the dye IR-26 which has since been found to be ten times too large[47,48].. We have confirmed this corrected value (0.05%) in our lab.

SWIR QDs that were administered by intravenous injection and exhibited different pharmacokinetics and biodistribution due to different biofunctionalization (figures 2b—h). A “green” SWIR QD (QD1080) was embedded in a lipid emulsion of large lipid droplets, which after the injection were found in the lungs and organs of the reticulo-endothelial system (RES) – mainly in the liver and spleen (figure 2b and 2f). The second sample of “red” SWIR QDs (QD1280) was incorporated into micelles formed out of PEG2000-phospholipids[19], which are roughly 25 nm in hydrodynamic diameter and are known to exhibit a long circulation time[20,21]. These “red” SWIR QDs stay in the blood after injection and all perfused organs show a signal in the red channel (figure 2c and 2g). The two channels can be merged (figure 2d and 2h) and a reflected light image can also be added for reference (figure 2e), generating a multiplexed color SWIR image.

## Metabolic Imaging with functionalized SWIR-QDs

We and others have recently incorporated visible light-emitting QDs into lipoproteins to follow their physiologic fate *in vivo*[22–26]. Lipoproteins, in particular triglyceride-rich lipoproteins such as chylomicrons, which are micron size micelles, carry dietary lipids absorbed by the intestine through the lymphatic system into the blood stream and deliver their cargo to peripheral tissues such as brown and white adipose tissue, skeletal muscle and the heart. Similar to glucose, triglyceride-rich lipoproteins are a major source of energy for tissues. Therefore SWIR-QD labelled lipoproteins should allow studying metabolic activity complementary to flurodeoxyglucose (18F) glucose positron emission tomography (FDG PET) imaging.

Existing methods such as MRI or radioactive labelling are limited by either their sensitivity and dynamic range or temporal resolution and invasive nature. The relative transparence of tissues at SWIR wavelengths enables tracking of labeled lipoproteins as they circulate and bind to the vasculature of target organs. Additionally, the relative lack of autofluorescence from these tissues enables the detection of low lipoprotein concentrations, and thus allows for quantification

within a large dynamic range. Brown adipose tissue (BAT) is a heat-producing organ, which in response to cold exposure fuels its high metabolic activity by the uptake of triglyceride-rich lipoproteins. To characterize this process, we exposed wild type mice (4 biological replicates) to 4°C for 24 hours to activate its BAT. After sedation and preparation, individual mice were illuminated with an 808 nm source (15 mW/cm$^2$), and were injected with SWIR QD-labeled recombinant chylomicrons via the tail vein at a constant rate of 26.7 µL/min for 9.3 minutes (0.267 mg triglycerides/min; figure 3a and supplementary video 2). During and after the injection we imaged the SWIR emission. After the experiment, we particularly analyzed the emission intensity arising from BAT, peripheral vasculature, and tail vein (figure 3b). The emission intensity in each region of interest provided a measure of the relative concentration of the labeled chylomicrons at that location, and halting the injection enabled capturing the kinetics of the physiological processes at play metabolizing these particles in each organ. This imaging paradigm was robust and technically highly reproducible as the variation between four separate mice was largely determined only by biological variation between mice (supplementary figure 6), and in figure 3b we overlay the results to show the reproducibility and biological variation between individual mice.

From these kinetic traces we were able to measure the blood half-life and rate at which chylomicrons are released from the BAT as chylomicron remnants. After the injection into the tail was halted the particles cleared from the blood and the signal decay for peripheral vasculature is fit well by a sum of two exponential functions and a constant. The blood half-life was on the order of 1 minute (73 s +/- 1 s; 42 s +/- 1 s; 70 s +/- 3 s; 58 s +/- 3 s) which is in agreement with previously reported values for cold exposed mice based on radioactive labeling[23]. The signal from the BAT decayed significantly slower and is fit well by a sum of two exponential functions. The signal remaining in the BAT revealed that initial release of chylomicrons remnants, the product of lipolysis, from this tissue occurs with a time constant of

about 3 minutes (196 s +/- 5 s; 83 s +/- 1 s; 195.5 s +/- 0.5 s; 241.0 s +/- 0.5 s; roughly half of the bound chylomicron population was cleared in this way). This is followed by a much slower decay on a time scale of greater than 30 minutes (roughly half of the bound chylomicron population showed this behavior). The long residence time is consistent with recent reports noting the existence of long-term uptake of particles[23]. The particles released from the BAT and other peripheral tissues got cleared by the liver.

The SWIR region thus offers three benefits: First, the longer penetration length allows us to resolve the image of organs deep in a mouse; Second, as tissues are translucent in this region, small concentrations of SWIR QDs can be detected with high temporal resolution even with a relatively low excitation flux; and, finally, the relative absence of tissue autofluorescence enables the detection of low concentrations and thus allows quantification over a large dynamic range (supplementary figure 7).

## High-speed SWIR whole body imaging

The high QY of our QDs, coupled with the fact that tissues are translucent in the SWIR, gives rise to high emission signals even under low excitation fluxes. This allows us to image at acquisition speeds of up to 66.5 frames per second (fps) — limited not by signal but by the readout electronics of our camera — while retaining high resolution. We achieved an acquisition speed more than twice as fast and a resolution with four times more pixels compared to previous reports for imaging in the SWIR[10]. Figure 4 and supplementary videos 3—5 show whole body imaging of mice, both anesthetized as well as awake and unrestrained, demonstrating the high speed and high signal-to-background ratio of our SWIR QDs. Indeed, we measured a signal for the heart and liver that is more than two orders of magnitude higher than background autofluorescence, and a signal-to-noise ratio for the liver of about 24 dB for our 640x512 pixel camera (figure 4b, supplementary videos 3 and 4). Both heartbeat and the respiratory cranio-caudal motion of the liver (figure 4b and supplementary video 4) are clearly

resolved. This representative anesthetized mouse shows a respiratory rate of 84 breaths per minute (figure 4c) and a heart rate of 130 beats per minute (figure 4d).

Physiology however, is profoundly affected by anesthesia. Currently used approaches to record the heart rate in awake animals rely either on implanting telemetric sensors by surgery or by ECG after confining the animal in a device with conductive pads for recording. The emission of SWIR QDs signal can overcome this limitation and is in fact strong enough to study freely moving and awake mice, in contrast to stationary and anesthetized mice which are required for most other imaging techniques such as MRI, CT and US. We injected long-circulating PEGylated SWIR-QDs via the tail vein into awake mice and placed them into our imaging setup. After allowing the mice to acclimate, we imaged in the dark, reflecting their usual environment as a nocturnal species. Notably, the 808nm laser used in this experiment is invisible to mice, as their eyes are even less sensitive than humans to these wavelengths[27]. Figure 4e (supplementary video 5) demonstrates our ability to measure the heart and respiratory rates of a mouse, in a contact-free way and without restraining or otherwise affecting the mouse. The recorded heart and respiratory rates at rest of this representative mouse were 300 breaths per minute (figure 4f) and 550 beats per minute (figure 4g), in agreement with the literature[28,29] (SWIR-QD whole body imaging was performed for more than 10 mice).

*In vivo* imaging in the SWIR using high-QY QDs thus opens up the possibility of contact-free non-invasive physiological imaging of mice that are awake and undisturbed.

## One-photon excitation SWIR intravital microscopy

The SWIR region of the optical spectrum is also optimal for intravital microscopy. The SWIR region benefits from long wavelength excitation in the near-infrared (NIR) similar to multi-photon microscopy, allowing deep tissue penetration and relatively high excitation flux without tissue damage. But there is one important difference: Multi-photon microscopy relies on two or three

photons combining to create a non-linear excitation event in a fluorophore that then emits in the visible range. This process is seven to eight orders of magnitude less efficient than emission from single photon excitation. The ability to excite in the near-IR with a one-photon event and detect in the SWIR gives rise to bright emission at moderate excitation intensities (on the order of 10 W/cm$^2$ in our set-up). In comparison, the peak intensity in the focus of multi-photon microscopes is on the order of $10^6$–$10^{12}$ W/cm$^2$. Additionally we benefit from the virtual absence of tissue autofluorescence and the high transmission of the SWIR emission. This combination allows us to easily generate microscopic images at video rate at penetration depths similar to multi-photon microscopy with an epifluorescence approach.

We used these benefits of SWIR imaging with QDs to image a glioblastoma (GBM) tumor growing in a mouse brain through a transparent cranial window (figure 5a). In this experiment the tumor was pre-labeled by injection of the PEGylated SWIR-QD composite particles three days before imaging. Following relabeling, the tumor continued to grow for the duration of three days, and the long-circulating PEGylated SWIR-QD composite particles appeared to accumulate in the collapsed and abnormal tumor blood vessels (figure 5b). A second dose of the PEGylated SWIR-QD composite particles was injected and perfusion was imaged at video-rate across the entire cranial window (30 fps, supplementary video 6). The time series of images was then deconvolved into the pre-labelled tumor (figure 5b), the arterial vessels (figure 5c) and the venous vessels (figure 5d), using a form of principal component analysis[30]. The resulting color-coded image (figure 5e) demonstrates how the growing tumor affects the vascular network.

We further demonstrate here that our PEGylated SWIR-QD composite particles allow detailed and quantitative imaging of blood flow in relatively large tissue volumes. Quantification of blood flow in the brain is of great importance as it serves as a surrogate for metabolic activity (e.g. in functional MRI (fMRI)). Aberrant blood flow in diseases ranging from cancer to stroke often

leads to hypoxia. Current approaches to measure blood flow either lack the spatial resolution to resolve individual capillaries (e.g. fMRI) or are too slow to acquire flow information of large volumes (e.g. line-scanning multi-photon microscopy[31]).

Z-sectioned images of abnormal and normal vasculature in the same mouse (figure 6a) were generated by imaging the dynamics of the flow in healthy tissue (supplementary video 7) and in the tumor margin of a GBM (supplementary video 8). The GBM tumor margin showed irregular blood flow, including oscillatory “pendular” flow, while the healthy tissue in the contralateral brain hemisphere showed a normal vessel network with regular blood flow. Calculating the maximum projection of all frames visualized the overall structure of the vasculature in the tumor margin (figure 6b) and healthy tissue (figure 6c). The details of the vessel structure, however, were contaminated by out-of-plane information. Subtracting the average signal of these 600 frames from the maximum intensity projection isolated the signal in the focus originating only from individual QD-SWIR composite particles (figures 6d and 6e).

In another approach to enhance the contrast of the focal plane and provide true z-sectioning capability, we calculated the sum of the magnitude of the difference of each frame from the average, which is sensitive only to fluctuations over time, i.e. the transit of individual composite particles. The static z-sectioned images produced in this fashion are comparable to equivalent images produced using multiphoton microscopy (MPM). Figures 6f—k directly compare the micrographs of the same fields of view of a healthy mouse brain at various depths, using our novel z-sectioning approach (figures 6f—h) and conventional MPM (figures 6i—k).

It is important to note that we also exploited the high spatiotemporal resolution of our data to perform particle image velocimetry (PIV)[32–35], yielding z-sectioned measurements of the flow of blood through the vasculature at 5 µm increments (figure 7 and supplementary video 9). By combining static images of the vasculature (figures 7a and 7c, supplementary videos 10 and 11)

with their flow information (figures 7b and 7d), we generated a quantitative three-dimensional representation of blood flow in the brain (supplementary video 12) for this representative mouse (SWIR-QD intravital microscopy with composite particles was repeated for different organs in more than ten mice). Each z-section requires 10 sec of experimental time, so that large volumes of brain tissue may be mapped in minutes. The high spatial and velocity resolution of our flow maps arise directly from our ability to accurately measure the displacement of individual particles over time, which is only achievable by the use of bright and compact labels, such as those composed of SWIR QDs.

## Discussion

SWIR *in vivo* fluorescence imaging was introduced as a spectral regime rendering living tissue translucent. For example it has previously allowed the observation of brain vasculature through skin and skull of mice[3]. However, the lack of a versatile SWIR emitter technology has prevented the general adoption of SWIR *in vivo* imaging despite its advantages over visible and near-IR imaging. Here, we demonstrate that using core/shell SWIR QDs as a functionalizable probe with high QY allows for biomedical *in vivo* imaging of both sedated and awake animals. The use of our SWIR biofunctional platform yields detailed information about mouse physiology, metabolism, and pathologic processes such as tumor vascularization.

The deep penetration of SWIR emission and the low levels of background enable us to directly measure the metabolic activity of different tissues in a mouse, by tracking lipoproteins labelled with SWIR QDs. In contrast to existing methods based on radioactive labelling our technique allows measuring the kinetics with a precision of a few seconds that exceeds the biological variation between mice of the same group (on the order of tens of seconds). With this method it is now possible to completely measure, in real-time and with high dynamic range, lipoprotein processing for several organs simultaneously in individual mice. We anticipate future work in which the individual mechanisms of binding and uptake can be analyzed in greater detail in individual animals, possibly reducing the required amount of biological replicates for quantification studies. It is also possible to assess the real-time effects of an intervention within an individual animal, such that the results are purely reflective of the effects on the individual and not biased by differences within the population. This approach is not limited to lipoproteins but can be expanded to study the binding kinetics of therapeutic antibodies or other biomolecules.

The orders-of-magnitude improvement of signal that QDs provide, relative to existing SWIR probes, enables imaging physiological processes that are otherwise too fast to be detected by common imaging methods such as MRI or near-infrared fluorescence imaging. In this report we demonstrate the measurement of the heartbeat and breathing rates of an awake and unrestrained mouse, paving the way for automated and unobtrusive monitoring of animals in their normal environments. This method could be applied to test drug candidates for cardiac arrhythmia, for which SWIR imaging would enable researchers to monitor the animals over time without the need to implant telemetric devices. The ability to non-invasively monitor vital signs would also be beneficial for studies of exercise and behavior, where it is critical to ensure that the animal is in a normal and unstressed state.

In a microscopic setting the strong signal of our QDs enables the measurement of blood flow in the vasculature of the brain. With such a method, it is possible to characterize the flow in large volumes of vasculature in only a few minutes of experimental time, for example before and after an intervention to study ischemia-reperfusion in stroke. The applications, however, are not limited to pathological processes: almost every tissue can switch between a baseline, resting state and an activated state of enhanced functional performance (motion of a muscle, lipolysis of white adipose tissue, heat production by BAT) with increased perfusion. Similar to functional MRI but with much higher spatial and temporal resolution our technique of flow measurement may allow quantification and tracking of the activation of certain areas of the brain by detecting changes in blood flow in response to external stimuli.

Central to all of these applications is the ability to appropriately functionalize QDs. Even an emitter with superior optical properties is rendered useless if it cannot be tailored for a given application. The widespread adoption of SWIR *in vivo* imaging will only be enabled by the further development of a complete functional library akin to that which exists for visible probes. While we did not observe toxic effects in mice during our short-term studies we realize that the

chemical composition of our SWIR-QDs might prohibit the use in humans. Thus the development of heavy metal-free, high quality SWIR emitters will be the next challenge in order to bring SWIR imaging into clinical settings. In the meantime, our versatile and compact probes open an avenue toward the broader application of SWIR imaging in biomedical research.

## Acknowledgements

This work received support from the NIH in part through 5-U54-CA151884 (M.G.B.), P01-CA080124 (R.K.J. and D.Fukumura), R01-CA126642 (R.K.J.), R01-CA096915 (D.Fukumura), the NIH funded Laser Biomedical Research Center through 9-P41-EB015871-26A1 (M.G.B.), and NCI/Federal Share Proton Beam Program Income (R.K.J.); the ARO through the Institute for Soldier Nanotechnologies (W911NF-13-D-0001; O.C., H.W., G.W.H., M.G.B.); the Department of Defense through DoD W81XWH-10-1-0016 (R.K.J.); and the NSF through ECCS-1449291 (D.Franke, M.G.B.). This work was supported as part of the MIT Center for Excitonics, an Energy Frontier Research Center funded by the U.S. Department of Energy, Office of Science, Office of Basic Energy Sciences under Award Number DE-SC0001088 (T.S.B., M.W.B.W.). O.T.B. is supported by an EMBO long-term fellowship. A.B. is supported by a Deutsche Forschungsgemeinschaft Research Fellowship (BA 4925/1-1). D.Franke is supported by a fellowship of the Evonik Stiftung and fellowship of the Boehringer Ingelheim Fonds. J.H. is supported by a grant from the Fondation Leducq - Triglyceride Metabolism in Obesity and Cardiovascular Disease. L.R. is grateful for the Mildred-Scheel-Stipendium from the Deutsche Krebshilfe. D.K.H. and D.M. were supported by NSF GRFP fellowships. J.K. was supported by fellowships from the Deutsche Forschungsgemeinschaft and the SolidarImmun Foundation. CJR and PTCS acknowledge support from NIH -5-P41-EB015871-27, DP3-DK101024 01, 1-U01-NS090438-01, 1-R01-EY017656 -0, 6A1, 1-R01-HL121386-01A1, the Biosym IRG of Singapore-MIT Alliance Research and Technology Center, the Koch Institute for Integrative Cancer Research Bridge Initiative, Hamamatsu Inc., and the Samsung GRO program.

We thank Sylvie Roberge and Peigen Huang for technical assistance. We are grateful to Gökhan Hotamisligil for critical discussion and continuing support.

# Methods

## Synthesis of InAs core/shell QDs

### Synthesis of InAs cores

In a typical procedure, 4 mmol of indium(III) acetate, 14 mmol myristic acid, and 20 mL 1-octadecene were added to a 50 mL 4-neck round bottom flask. The flask was heated to 110°C under vacuum (10 mtorr) for two hours to remove acetic acid and form a solution of indium(III) myristate. The indium myristate solution was heated under argon to 295°C. An injection syringe containing 0.22 mmol tris(trimethylgermyl)arsine dissolved in 4 mL tri-n-octylphosphine was prepared in a nitrogen glovebox and rapidly injected into the indium myristate solution at 295°C. After 10 minutes, a syringe containing 0.72 mmol tris(trimethylgermyl)arsine dissolved in 1 mL tri-n-octylphosphine and 4 mL 1-octadecene was loaded into a syringe pump and the arsenic precursor solution was injected at 4mL/hour at a temperature of 295°C. The QD size was monitored during this step by removing aliquots from the solution. When the QDs reached the desired size, the precursor injection was stopped and the reaction was removed from heat.

The QDs were isolated by filtering the growth solution diluted in toluene through a 200nm PTFE filter, then adding acetone to cause the QDs to precipitate out of solution and centrifuging. The QDs were dissolved in 20mL hexane and stored for overcoating.

### Overcoating InAs cores

#### *InAs/CdSe/ZnSe*

The ZnSe overcoating procedure is adapted from a published method[36]. 44 nmol of InAs cores in hexane were added to 4 mL of 1-octadecene, 3 mL of oleylamine, and 0.5 mL of 0.05 M

trioctylphosphine selenide in TOP (TOPSe). The solution was degassed at 100°C under vacuum for 40 minutes, 15 mtorr, to remove the hexane, and then heated to 230°C under argon. 0.47 mL of solutions of 0.05 M cadmium oleate and 0.05 M TOPSe were injected side by side using a syringe pump at 1 mL/hr at 230°C. Then 0.6 mL of 0.05 M diethylzinc was added and the temperature was raised to 250°C. After 15 minutes, 0.6 mL of 0.05 M TOPSe was added. After 15 minutes, 0.75 mL of 0.05 M diethylzinc was added. After 10 minutes, 0.95 mL of 0.04 M Se dissolved in ODE was added. After 15 minutes, 1 mL of oleic acid was injected. After 13 minutes, 0.95 mL of diethylzinc was added. After another 13 minutes, 1.2 mL of 0.04 M ODE-Se was added. The temperature was raised to 290°C for 25 minutes and then the reaction mixture was cooled. The quantum yield was found to be 30% using an integrating sphere. The PL peak was around 1075 nm.

### *InAs/CdS*

This procedure is adapted from conditions described for making CdSe/CdS core/shell QDs[37]. 90 nmol of InAs cores in hexanes were added to 10 mL of ODE. The solution was degassed under vacuum at 100°C to remove the hexane. 8.2 mL of 0.05 M solutions of cadmium oleate and sulfur in 1-octadecene were added side by side using a syringe pump at 5 mL/hr at a temperature of 230°C. The PL peak was found to be 1150 nm, with a quantum yield of 35% in chloroform.

## Synthesis of PbS/CdS core/shell QDs

PbS is synthesized with lead oleate as a Pb precursor, hexamethyldisilithiane (as known as $(TMS)_2S$) as a S precursor, and 1-octadecene as a solvent[38]. All the syntheses were performed under an inert atmosphere. Lead oleate is prepared using lead acetate trihydrate and oleic acid at 120 $^{o}$C, then the lead precursor is heated to 150 $^{o}$C under nitrogen before injection of the sulphur precursor. After cooling to room temperature, this solution is transferred into a nitrogen-filled glove box without air exposure. The synthesized PbS QDs are purified three times by

adding methanol and 1-butanol until the solution is turbid, followed by centrifugation to precipitate the QDs. The supernatant is discarded and the QDs are re-dissolved in hexane. PbS/CdS core/shell QDs are prepared by cation-exchange[39,40] at 100 $^{o}$C for 5 min under nitrogen using an excess of cadmium oleate. PbS/CdS core/shell QDs are also precipitated with ethanol and re-dissolved into hexane three times to purify and remove unreacted precursors.

## Transfer of QDs from organic solvents into aqueous buffers

### Formation of PEG-phospholipid micelles

QDs were transferred into aqueous buffers using a previously reported procedure[19,20]. Briefly, 3 mg (dry weight) QDs were mixed with 25 mg 18:1 PEG2000 PE (1,2-dioleoyl-sn-glycero-3-phosphoethanolamine-N-[methoxy(polyethylene glycol)-2000]) (ammonium salt) (Avanti Polar Lipids; Cat.No 880130) in chloroform. After brief sonication for 10 seconds the solvent was removed under nitrogen flow and 2 mL isotonic saline or water were added. To completely solubilize the QDs the aqueous solution was sonicated with a probe sonicator for 5 min. This solution was filtered through a 0.2 µm filter.

### QD-labelled recombinant triglyceride rich lipoproteins

QD-labelled recombinant triglyceride rich lipoproteins were generated by a previously reported procedure[22,23]. Briefly, physiological lipoprotein extracts from triglyceride rich lipoproteins (TRL) were extracted by the method of Folch[41]. For incorporating the QDs into the recombinant lipoproteins, 20 mg of the lipid extract (approximately 80% triglycerides, 10% cholesterol and 10% phospholipids) were dissolved in chloroform and mixed with 1 mg (dry weight) InAs core/shell nanocrystals. The solvent was removed and TRL were formed in 2 mL PBS or isotonic saline by sonication with a probe sonicator for 10 minutes. Potential aggregates were removed by filtration using a 0.45 µm filter prior to intravenous injection (2 mg lipid per mouse).

### PEGylated SWIR-QD composite particles

To obtain composite particles with a long circulation time 8 mg (dry weight) QDs were mixed with 5 mg 18:1 PEG2000 PE (1,2-dioleoyl-sn-glycero-3-phosphoethanolamine-N-[methoxy(polyethylene glycol)-2000]) (ammonium salt) (Avanti Polar Lipids; Cat.No 880130), 80 mg soy bean oil and 1.4 mg phosphatidylcholine in chloroform. After brief sonification for 10 seconds the solvent was removed under nitrogen flow and 2 mL isotonic saline were added. To form an emulsion of composite particles the aqueous solution was sonicated with a probe sonicator for 10 minutes. This solution was filtered through a 0.45 µm filter, yielding a solution of particles which were roughly 400 nm in diameter with a broad size distribution.

See supplementary table 1 for results of characterization of the different functionalizations.

## Optical characterization of QDs

### Photoluminescence quantum yield (QY)

Quantum yield measurements were obtained using an integrating sphere (Labsphere RTC-060-SF). The sample was illuminated using a 785nm diode laser with an excitation power of 25mW that was chopped at 210 Hz. The output was collected using a calibrated germanium detector (Newport: 818-IR) through a Stanford Research Systems lock-in amplifying system. An 800 nm colored glass longpass filter was used to block the excitation beam. The sample was placed in a PTFE capped quartz cuvette and a solvent blank was used to ensure as uniform of an environment inside the integrating sphere as possible. The measured photocurrent was adjusted to account for the external quantum efficiency of the detector when calculating the quantum yield. Finally, the measured quantum yield was corrected to account for leakage of the excitation light and the transmittance of the filter.

### Photoluminescence spectroscopy

For samples with emission peaks between 900 nm and 1300 nm, a single-grating spectromter (Acton; SpectraPro 300i) was used in conjunction with a liquid nitrogen cooled InGaAs line camera (Princeton Instruments; OMA V, 512x1 pixels). Samples were excited with a 532 nm diode laser, and emission was collected using a pair of gold-coated off-axis parabolic mirrors.

## Photoluminescence lifetime

To measure photoluminescence dynamics by time-correlated single-photon counting (TCSPC), samples (solutions in glass vials) were excited by a train of 532 nm, 100 ps-duration pulses at a repetition rate of 100 kHz generated by a laser diode (PicoQuant; LDH-P-FA-530B). The considerable waiting time between pulses (10 μs) ensured that the delayed fluorescence – consistent with long-lived 'trap' states on the nanocrystals – decayed below the noise floor of the detector ($<10^{-3}$ of the peak signal under these conditions). The pump was attenuated to yield roughly 1 nW of average excitation power, with a roughly 20 μm diameter excitation spot at the sample. Under these low-fluence excitation conditions, the photoluminescence decay dynamics were independent of excitation intensity. Accordingly, we consider bimolecular recombination channels to be unimportant.

The emission from the nanocrystals was collected and imaged onto an InGaAs/InP single-photon counting avalanche photodiode (Micro Photon Devices; $IR-DH-025-C), fitted with a long-pass filter (Chroma Technology Corp.; EP900LP) to suppress the scattered photons from the visible pump. The detector was operated asynchronously from the laser source, with a 2 MHz gate frequency and a 90% duty cycle. Using a PicoQuant PicoHarp and standard software, a decay trace histogram was generated by correlating the times of detection events with the proximal trigger from the pump laser. The time resolution, judged from the onset of the response to unfiltered pump scatter, was ~300 ps. This stemmed primarily from the uncertainty in the detector response at the low over-voltages required for low-noise operation. After

verifying that no rapid dynamics were observed, 256 ps time bins were used during data collection.

## Animal procedures

### Animal model and cell line

Murine Gl261 cells (Gl261 WT) were originally provided by the Frederick National Laboratory (NCI, Frederick, MD). Gl261-GFP-Gluc cell line was generated by transducing Gl261 WT cells with a bicistronic lentivirus vector (under the control of the constitutive cytomegalovirus promoter) containing both green-fluorescent-protein (GFP) and Gaussian-luciferase (GFP-Gluc) genes separated by an internal ribosomal entry site element[42], provided by the MGH vector core. All cells were grown in serum free conditions using the NeuroCult NS-A proliferation kit (Stemcell technologies, Vancouver, Canada) and maintained in a humidified atmosphere of 5% $CO_2$ and 95% air at 37°C. Gl261-GFP-Gluc cells were repeatedly tested negative for mycoplasma using the Mycoalert Plus Mycoplasma Detection Kit (Lonza) and authenticated before use by IDEXX laboratories (North Grafton, MA).

Approximately 200,000 tumor cells were implanted stereotactically into the left striatum of 8—10 week old male C57BL/6 mice (Gl261-GFP-Gluc) 2 mm left of the sagittal suture, 0.1 mm rostral of the bregma and at 2 mm depth from the brain surface[43,44]. Intravital images were taken through cranial windows.

### Cold exposure to activate brown adipose tissue

Mice were housed at 22°C with ad libitum access to standard laboratory chow diet. Cold exposure (4°C) was performed in single cages for 24 h. We used male 12 weeks old C57BL/6 (Charles River Laboratory) wild-type mice, which were fasted for the last 4 h before the imaging experiment. For *in vivo* imaging to measure metabolic rates mice were anesthetized and SWIR-

QD-labeled lipoproteins were injected via a tail vein catheter with a syringe pump (at a rate of 13.3 µL/min).

Animal experiments were conducted in accordance with approved institutional protocols of MGH and MIT.

## SWIR imaging apparatus

### Macroscopic imaging setup

For macroscopic imaging from above or below, we used two configurations of a single custom-built setup.

We coupled a 10 W 808 nm laser (Opto Engine; MLL-N-808) in a 910 µm-core metal-cladded multimode fiber (Thorlabs; MHP910L02). The output from the fiber is passed through a ground-glass plate (Thorlabs; DG20-220-MD) to provide uniform illumination over the working area. The excitation flux in this configuration is around 15mW/cm$^2$. The working area is comprised of a plate of clear glass affixed atop four 1 in pillars, 6 in off the table for illumination from above or 12 in off the table for illumination from below.

We used a 4 in square first-surface silver mirror (Edmund Optics; Part No 84448) to direct the emitted light through various filters (Thorlabs, Edmund Optics) to a Princeton Instruments Nirvana equipped with various C-mount camera lenses (Navitar). The whole assembly was surrounded by a partial enclosure to eliminate excess light while enabling manipulation of the field of view during operation.

For imaging of the vasculature of the brain through skin and skull we used a custom build setup to lenses (Thorlabs AC254-100-C and AC254-75-C) with a 1" silver elliptical mirror (Thorlabs PFE10-P01) and different long- and bandpass filters (Thorlabs and Edmund Optics) in between.

## Microscopic imaging setup

We used a Nikon Ti-E inverted microscope equipped with a Stage UP Kit (Nikon) and a backport adaptor. For illumination we used a 808 nm laser diode coupled to a fiber which was attached to the backport adaptor. To eliminate laser speckle we used an optune speckle remover (Edmund Optics; 88-397). We used a dichroic filter (Thorlabs; DMLP900R) to direct the excitation light to the sample and a 1000 nm longpass filter (Thorlabs; FELH1000,) to select the emission light. Imaging was done with a 10X (Nikon; CFI Plan Apo Lambda) or a 2X (Nikon; CFI Plan Apo Lambda,) objective. The PI Nirvana camera was attached to the sideport of the microscope. The camera was cooled to −80°C for imaging, the AD conversion rate was set to 10 MHz, the gain set to high, with different exposure times resulting in different frame rates.

## Metabolic imaging with functionalized SWIR-QDs

The mice were prepared as described in this report. For the resulting images we defined regions of interest representing the tail injection site, interscapular brown adipose tissue (BAT), and liver. The total intensity contained within each region of interest was determined and used to produce the time series data. A constant background was removed from each time series, based on the intensities of background fluorescence at the beginning of injection.

To fit the signal from the BAT, we identified the time point when the injection was halted, and noted the intensity of the signal from that point to the end of the experiment. We modeled the signal as a sum of three exponential functions, two of which had positive amplitude representing loss of signal, and a third with negative amplitude representing residual gain of signal due to the injection.

## Fluorescence angiography

We used our microscopic imaging setup with the 2X objective to image the brain of a mouse with a cranial window. We recorded a video (30fps) of the brain during injection of PEGylated QDs, three days after a similar injection to pre-label the tumor. Using this video we can perform a form of principal component analysis (PCA), using the PoissonNMF ImageJ plugin[45]. This method identifies the extent to which each pixel can be represented as an artery or vein by relating its temporal profile to those of vessels of known identity. Any signal existing before the imaged injection was assigned to be the background and pre-labeled tumor, from which we removed a laser speckle artifact by a form of flat field correction by combining multiple pictures taken with different fields of view before the injection. The color image in figure 5e represents the overlay of pre-injection, artery, and vein characters.

## Multiphoton microscopy

Fluorescein isothiocyanate–dextran/phosphate buffered saline solution (FITCDextran) was prepared for in vivo vessel tracing in a concentration of 10 mg/mL. Following tail vain injection of 100 µL of FITC-Dextran, a vessel image was acquired using multiphoton imaging described previously[43] on a custom-built multiphoton laser-scanning microscope using confocal laser-scanning microscope body (Optical Analysis Corp.; Olympus 300) and a broadband femtosecond laser source (Spectra-Physics; High Performance MaiTai). Image slices were taken with 300 mW at a wavelength of 810 nm. Imaging studies were performed with a 20X magnification, 0.95NA water immersion objective (Olympus XLUMPlanFl, 1-UB965, Optical Analysis). Image analysis was carried out using ImageJ.

## Particle image velocimetry

The PIV code was written in Matlab 2015a and is available here: https://github.com/massivehair/PIV

Firstly, the image stack is segmented into two regions, one containing flow and the other, background. This is achieved by first smoothing every frame in the stack using a Gaussian smoothing kernel with a sigma parameter of 2 pixels. The standard deviation of each X,Y position in the stack is taken, as a measure of the amount of motion in that part of the image. Finally, a grayscale image erosion operation using a disk kernel with a diameter of 25 pixels is used to reduce the influence of noisy pixels and isolated high-variance regions of the image. A threshold could then be selected to distinguish flowing regions from background. Since the effect of this threshold (and the prior steps) is to reduce the computational load of calculating large areas in which there is no flow, the algorithm is not especially sensitive to the choice of smoothing kernel, or threshold that is too low; any errors will simply reduce computational efficiency. For the data presented in figure 7 a threshold of 0.2 was used.

To perform the PIV calculation, firstly, each frame is smoothed using a Wiener filter with a filter size of 5 pixels on a side. A window size and maximum step size are defined. In the case of the data presented in figure 7 the window size is 8 pixel and the step size 40 pixel. Flow is calculated at grid locations spaced by the window size, provided these locations contain flow information (as assessed by the threshold previously applied). To calculate flow, two sub-images are taken from consecutive frames. One is taken from the first frame, centered on each grid location, with a size given by the window size. The second is taken from the subsequent frame, centered on the same grid location, with a size equal to the sum of the window size and the maximum step size. A cross-correlation is then taken between the two sub-frames; this is termed the correlation map. This is repeated for every grid locations, resulting in $n$-1 correlation maps for each, where $n$ is the number of frames in the stack.

Correlation maps were averaged across all frames, following the method of Meinhart, Wereley and Santiago[46], and then the peak corresponding to the modal flow vector located using a three-point Gaussian estimator[47].

## References


1. Welsher, K. *et al.* A route to brightly fluorescent carbon nanotubes for near-infrared imaging in mice. *Nat. Nanotechnol.* **4,** 773–80 (2009).

2. Yi, H. *et al.* M13 phage-functionalized single-walled carbon nanotubes as nanoprobes for second near-infrared window fluorescence imaging of targeted tumors. *Nano Lett.* **12,** 1176–83 (2012).

3. Hong, G. *et al.* Through-skull fluorescence imaging of the brain in a new near-infrared window. *Nat. Photonics* **8,** 723–730 (2014).

4. Ghosh, D. *et al.* Deep, noninvasive imaging and surgical guidance of submillimeter tumors using targeted M13-stabilized single-walled carbon nanotubes. *Proc. Natl. Acad. Sci. U. S. A.* **111,** 13948–53 (2014).

5. Bardhan, N. M., Ghosh, D. & Belcher, A. M. Carbon nanotubes as in vivo bacterial probes. *Nat. Commun.* **5,** 4918 (2014).

6. Welsher, K., Sherlock, S. P. & Dai, H. Deep-tissue anatomical imaging of mice using carbon nanotube fluorophores in the second near-infrared window. *Proc. Natl. Acad. Sci. U. S. A.* **108,** 8943–8 (2011).

7. Hong, G. *et al.* Multifunctional in vivo vascular imaging using near-infrared II fluorescence. *Nat. Med.* **18,** 1841–6 (2012).

8. Naczynski, D. J. *et al.* Rare-earth-doped biological composites as in vivo shortwave infrared reporters. *Nat. Commun.* **4,** 2199 (2013).

9. Lim, Y. T. *et al.* Selection of quantum dot wavelengths for biomedical assays and imaging. *Mol. Imaging* **2,** 50–64 (2003).

10. Hong, G. *et al.* Ultrafast fluorescence imaging in vivo with conjugated polymer fluorophores in the second near-infrared window. *Nat. Commun.* **5,** 4206 (2014).

11. Tsukasaki, Y. *et al.* Short-Wavelength Infrared Emitting Mutimodal Probe for Non-Invasive Visualization of Phagocyte Cell Migration in Living Mice. *Chem. Commun.* **50,** 14356–9 (2014).

12. Tao, Z. *et al.* Biological imaging using nanoparticles of small organic molecules with fluorescence emission at wavelengths longer than 1000 nm. *Angew. Chem. Int. Ed. Engl.* **52,** 13002–6 (2013).

13. Dong, B. *et al.* Facile Synthesis of Highly Photoluminescent Ag 2 Se Quantum Dots as a New Fluorescent Probe in the Second Near-Infrared Window for in Vivo Imaging. *Chem. Mater.* **25,** 2503–2509 (2013).

14. Zhu, C.-N. *et al.* $Ag_2Se$ quantum dots with tunable emission in the second near-infrared window. *ACS Appl. Mater. Interfaces* **5,** 1186–9 (2013).

15. Zhang, Y. Y. *et al.* Ag2S quantum dot: a bright and biocompatible fluorescent nanoprobe in the second near-infrared window. *ACS Nano* **6,** 3695–702 (2012).

16. Tsukasaki, Y. *et al.* Synthesis and optical properties of emission-tunable PbS/CdS core–shell quantum dots for in vivo fluorescence imaging in the second near-infrared window. *RSC Adv.* **4,** 41164–41171 (2014).

17. Chen, O. *et al.* Compact high-quality CdSe-CdS core-shell nanocrystals with narrow emission linewidths and suppressed blinking. *Nat. Mater.* **12,** 445–51 (2013).

18. Zhang, Y. *et al.* Biodistribution, pharmacokinetics and toxicology of Ag2S near-infrared quantum dots in mice. *Biomaterials* **34,** 3639–46 (2013).

19. Dubertret, B. *et al.* In vivo imaging of quantum dots encapsulated in phospholipid micelles. *Science* **298,** 1759–62 (2002).

20. Stroh, M. *et al.* Quantum dots spectrally distinguish multiple species within the tumor milieu in vivo. *Nat. Med.* **11,** 678–82 (2005).

21. Ducongé, F. *et al.* Fluorine-18-labeled phospholipid quantum dot micelles for in vivo multimodal imaging from whole body to cellular scales. *Bioconjug. Chem.* **19,** 1921–6 (2008).

22. Bruns, O. T. *et al.* Real-time magnetic resonance imaging and quantification of lipoprotein metabolism in vivo using nanocrystals. *Nat. Nanotechnol.* **4,** 193–201 (2009).

23. Bartelt, A. *et al.* Brown adipose tissue activity controls triglyceride clearance. *Nat. Med.* **17,** 200–5 (2011).

24. Heeren, J. & Bruns, O. Nanocrystals, a new tool to study lipoprotein metabolism and atherosclerosis. *Curr. Pharm. Biotechnol.* **13,** 365–72 (2012).

25. Fay, F. *et al.* Nanocrystal Core Lipoprotein Biomimetics for Imaging of Lipoproteins and Associated Diseases. *Curr. Cardiovasc. Imaging Rep.* **6,** 45–54 (2013).

26. Jung, C. *et al.* Intraperitoneal Injection Improves the Uptake of Nanoparticle-Labeled High-Density Lipoprotein to Atherosclerotic Plaques Compared With Intravenous Injection: A Multimodal Imaging Study in ApoE Knockout Mice. *Circ. Cardiovasc. Imaging* **7,** 303–11 (2014).

27. Jacobs, G. H., Neitz, J. & Deegan, J. F. Retinal receptors in rodents maximally sensitive to ultraviolet light. *Nature* **353,** 655–6 (1991).

28. Henry L. Foster, J. David Small, James G. Fox, E. *The Mouse in Biomedical Research: Normative Biology, Immunology, and Husbandry*. (Elsevier Science, 2014).

29. Berndt A, Leme AS, Paigen B, Shapiro SD, S. K. Unrestrained plethysmograph and anesthetized forced oscillation methods of measuring lung function in 29 inbred strains of mice. *MPD:35108. Mouse Phenome Database web site, The Jackson Laboratory, Bar Harbor, Maine USA. http://phenome.jax.org*

30. Hillman, E. M. C. & Moore, A. All-optical anatomical co-registration for molecular imaging of small animals using dynamic contrast. *Nat. Photonics* **1,** 526–530 (2007).

31. Kamoun, W. S. *et al.* Simultaneous measurement of RBC velocity, flux, hematocrit and shear rate in vascular networks. *Nat. Methods* **7,** 655–660 (2010).

32. Adrian, R. J. Twenty years of particle image velocimetry. *Exp. Fluids* **39,** 159–169 (2005).

33. Adrian, R. J. Particle-Imaging Techniques for Experimental Fluid Mechanics. *Annu. Rev. Fluid Mech.* **23,** 261–304 (1991).

34. Shi, Y., Cheng, J. C., Fox, R. O. & Olsen, M. G. Measurements of turbulence in a microscale multi-inlet vortex nanoprecipitation reactor. *J. Micromechanics Microengineering* **23,** 075005 (2013).

35. Schindelin, J. *et al.* Fiji: an open-source platform for biological-image analysis. *Nat. Methods* **9,** 676–82 (2012).

36. Aharoni, A., Mokari, T., Popov, I. & Banin, U. Synthesis of InAs/CdSe/ZnSe core/shell1/shell2 structures with bright and stable near-infrared fluorescence. *J. Am. Chem. Soc.* **128,** 257–64 (2006).

37. Li, J. J. *et al.* Large-scale synthesis of nearly monodisperse CdSe/CdS core/shell nanocrystals using air-stable reagents via successive ion layer adsorption and reaction. *J. Am. Chem. Soc.* **125,** 12567–75 (2003).

38. Hines, M. A. & Scholes, G. D. Colloidal PbS Nanocrystals with Size-Tunable Near-Infrared Emission: Observation of Post-Synthesis Self-Narrowing of the Particle Size Distribution. *Adv. Mater.* **15,** 1844–1849 (2003).

39. Pietryga, J. M. *et al.* Utilizing the lability of lead selenide to produce heterostructured nanocrystals with bright, stable infrared emission. *J. Am. Chem. Soc.* **130,** 4879–85 (2008).

40. Supran, G. J. *et al.* High-Performance Shortwave-Infrared Light-Emitting Devices Using Core–Shell (PbS–CdS) Colloidal Quantum Dots. *Adv. Mater.* **27,** 1437–42 (2015).

41. Folch, J., Lees, M. & Sloane Stanley, G. H. A simple method for the isolation and purification of total lipides from animal tissues. *J. Biol. Chem.* **226,** 497–509 (1957).

42. Wurdinger, T. *et al.* A secreted luciferase for ex vivo monitoring of in vivo processes. *Nat. Methods* **5,** 171–3 (2008).

43. Kodack, D. P. *et al.* Combined targeting of HER2 and VEGFR2 for effective treatment of HER2-amplified breast cancer brain metastases. *Proc. Natl. Acad. Sci. U. S. A.* **109,** E3119–27 (2012).

44. Kloepper, J. *et al.* Ang-2/VEGF bispecific antibody reprograms macrophages and resident microglia to anti-tumor phenotype and prolongs glioblastoma survival. *Proc. Natl. Acad. Sci. U. S. A.* **113,** 4476–81 (2016).

45. Neher, R. A. *et al.* Blind source separation techniques for the decomposition of multiply labeled fluorescence images. *Biophys. J.* **96,** 3791–800 (2009).

46. Meinhart, C. D., Wereley, S. T. & Santiago, J. G. A PIV Algorithm for Estimating Time-Averaged Velocity Fields. *J. Fluids Eng.* **122,** 285 (2000).

47. Marxen, M., Sullivan, P. E., Loewen, M. R. & Jähne, B. Comparison of Gaussian particle center estimators and the achievable measurement density for particle tracking velocimetry. *Exp. Fluids* **29,** 145–153 (2000).

48. Semonin, O. E. *et al.* Absolute Photoluminescence Quantum Yields of IR-26 Dye, PbS, and PbSe Quantum Dots. *J. Phys. Chem. Lett.* **1,** 2445–2450 (2010).

49. Hatami, S. *et al.* Absolute photoluminescence quantum yields of IR26 and IR-emissive Cd(1-x)Hg(x)Te and PbS quantum dots--method- and material-inherent challenges. *Nanoscale* **7,** 133–43 (2015).

## Figures

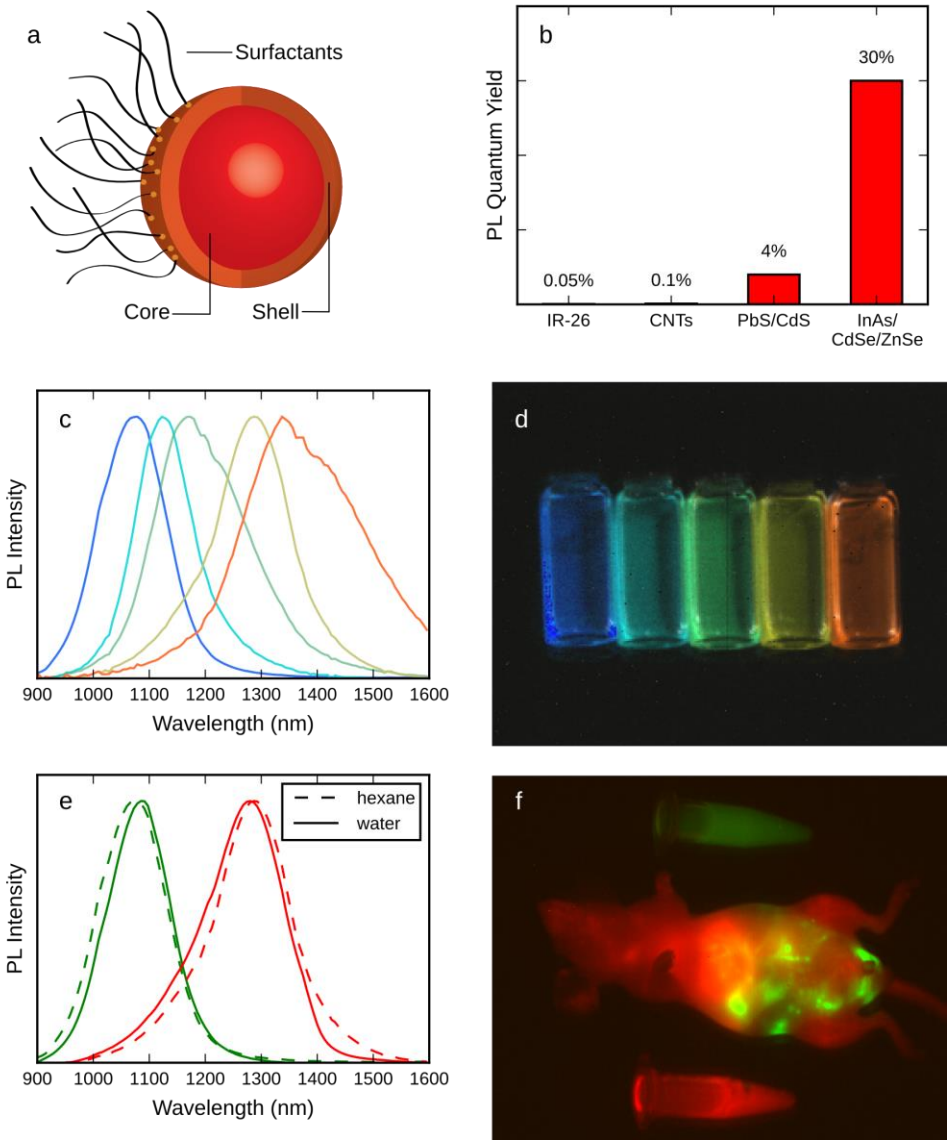


**Figure 1: InAs core/shell quantum dots with high quantum yield and size-tunable emission for functional and high-speed SWIR imaging.**

A schematic of core/shell SWIR quantum dots is shown in (a). Core/shell SWIR QDs exhibit a quantum yield in aqueous buffer of up to 30%, much higher than for previously-used materials (b)**Error! Bookmark not defined.** Spectra of five different core/shell SWIR QDs are shown (c). A spectral image of those five samples yields a pseudo-color SWIR image (d). The emission

spectra change only minimally after transfer into aqueous buffer (e). Two different SWIR-QDs were injected into a nude mouse intraperitoneally (green) and intravenously (red). A spectral image was taken and separated into red and green by linear unmixing (f).

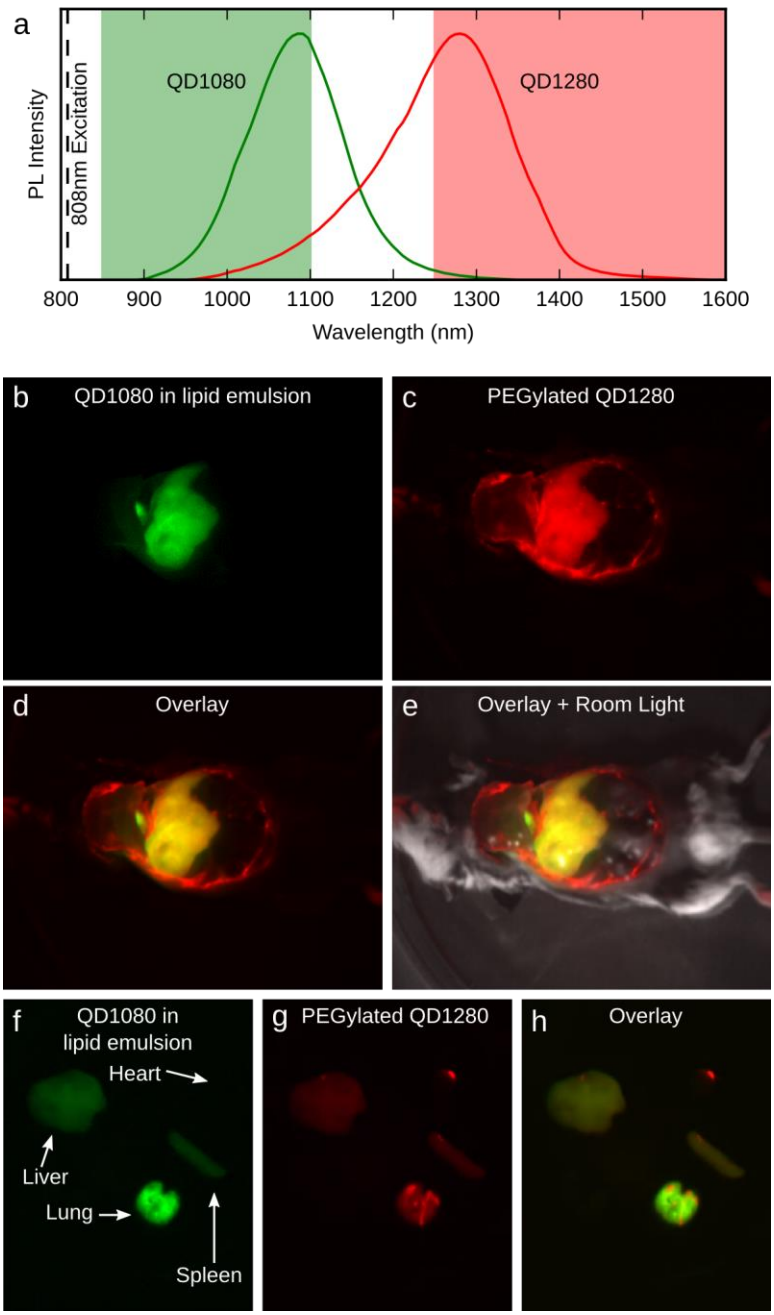


## Figure 2: Color QD-SWIR imaging for multiplexing and functional imaging.

(a) Two different SWIR QDs, color-coded green and red, were functionalized differently for multiplexing. SWIR-QDs in a lipid emulsion (QD1080) and PEGylated SWIR-QDs (QD1280) were subsequently injected into a mouse. The mouse was sacrificed and opened prior to color

SWIR imaging. The PEGylated SWIR-QDs (QD1280) were excited using an 808 nm laser and detected selectively with 1250 nm longpass filter (b) and the SWIR-QDs in a lipid emulsion (QD1080) were imaged with the combination of a 850 nm longpass and a 1100 nm shortpass filter (c). The overlay of both is shown in (d) and an overlay with an additional reflected light picture in grayscale is shown in (e). The organs were excised and the pictures for lipid emulsion (QD1080) (f), PEGylated SWIR-QDs (QD1280) (g) and the overlay (h) are shown.

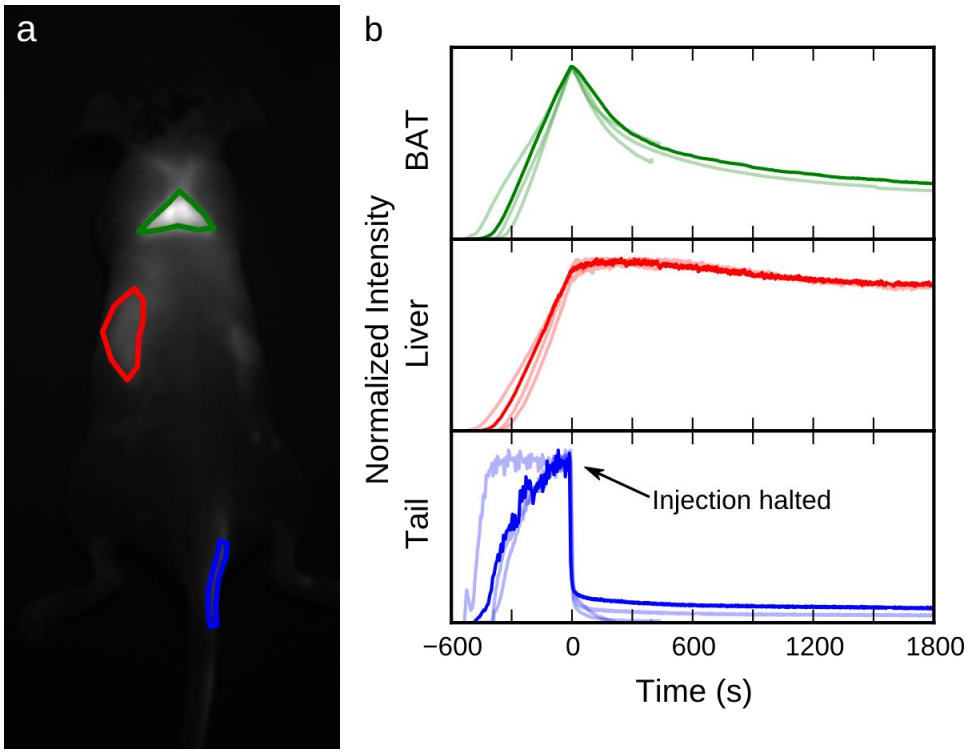


**Figure 3: SWIR-QDs for functional and metabolic imaging**

(a) A solution of a SWIR QD labeled recombinant chylomicrons was injected at a constant rate (26.7 µL/min or 0.267 mg triglycerides/min) into the tail vein of a cold-exposed mouse. The mouse was illuminated using an 808 nm laser with 15 mW/cm$^2$, and the SWIR emission was measured for the brown adipose tissue (BAT), liver and tail vein. (b) This process was repeated for four mice, with the darkened curves representing the results from the one mouse shown in (a), and the lighter curves showing the qualitative similarity of the other mice. The BAT signal after the injection revealed two distinct timescales for clearance: the initial signal loss is consistent with binding and release (about 3 minute time constant, 50% of the signal), while the longer-term component is consistent with uptake (>30 minute time constant).

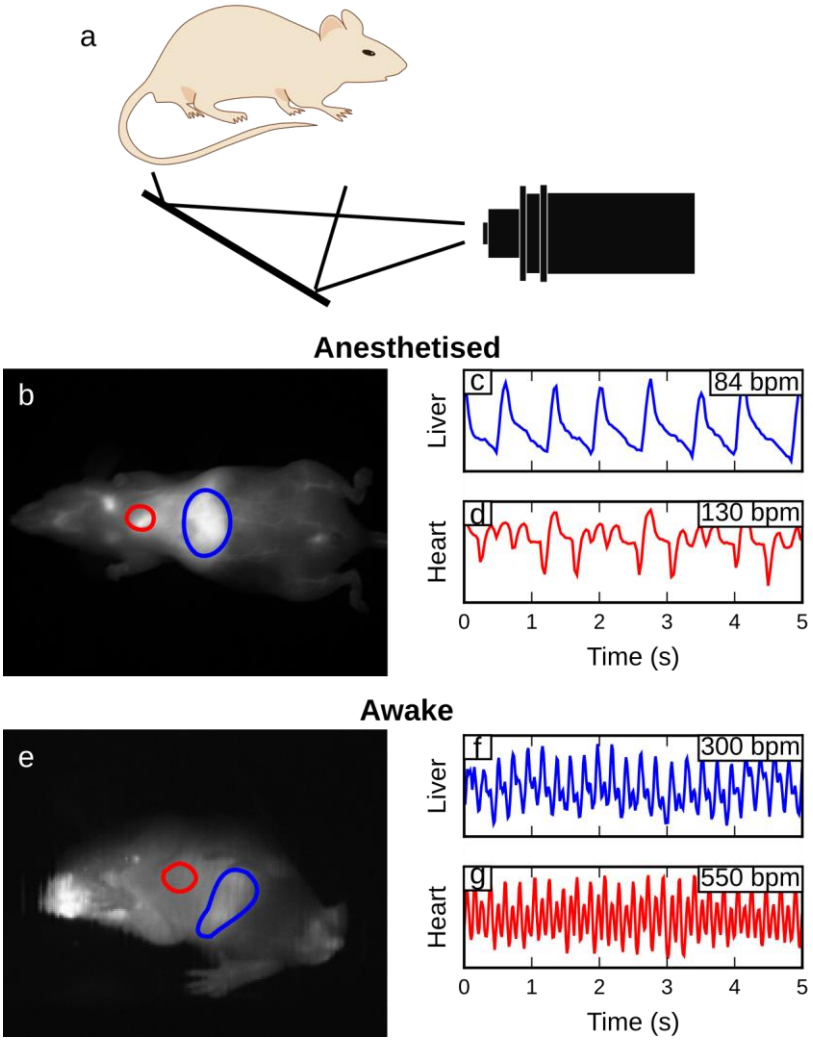


**Figure 4: High-speed QD-SWIR imaging for contact free monitoring of heart and respiratory rate in anesthetized and awake mice.**

Imaging in ventral orientation (a) at video-rate (30 fps; supplementary video 4) with SWIR-QDs (808 nm excitation) allows imaging vital signs like heart rate (red ROI) and respiration (blue ROI). (b) The respiratory rate of this anesthetized mouse is 84 breaths per minute (c) and the heart rate is 130 beats per minute (d). The bright emission of our SWIR-QDs allows the imaging of an awake mouse (66.5 fps; supplementary video 5) and the detection of the signal fluctuations generated by motion of liver and heart (e). A respiratory rate of 300 breaths per

minute (f) and a heart rate of 550 beats per minute (g) is observed in this awake but resting mouse.

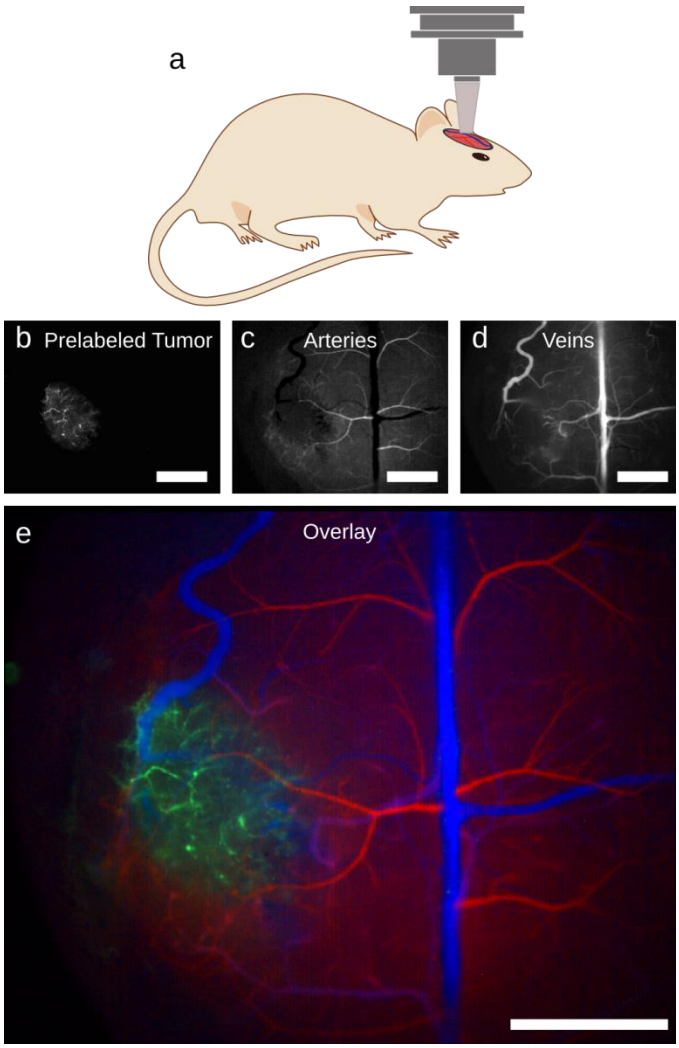


## Figure 5: High-speed QD-SWIR intravital imaging

SWIR intravital imaging (808 nm excitation, 1000nm long pass for emission) in a mouse with a cranial window (a) bearing a glioblastoma multiforme (GBM) in the left hemisphere of the brain as shown in (b). Principal component analysis (PCA) was used to distinguish arterial (c) from venous vessels (d) in the brain. This information is color-coded creating a multicolor angiograph (e) showing the abnormalities of the tumor microvascular network as opposed to normal arterial/venous brain vasculature (green: tumor; red: arterial vessels; blue: venous vessels). Scale bars are 1500 μm.

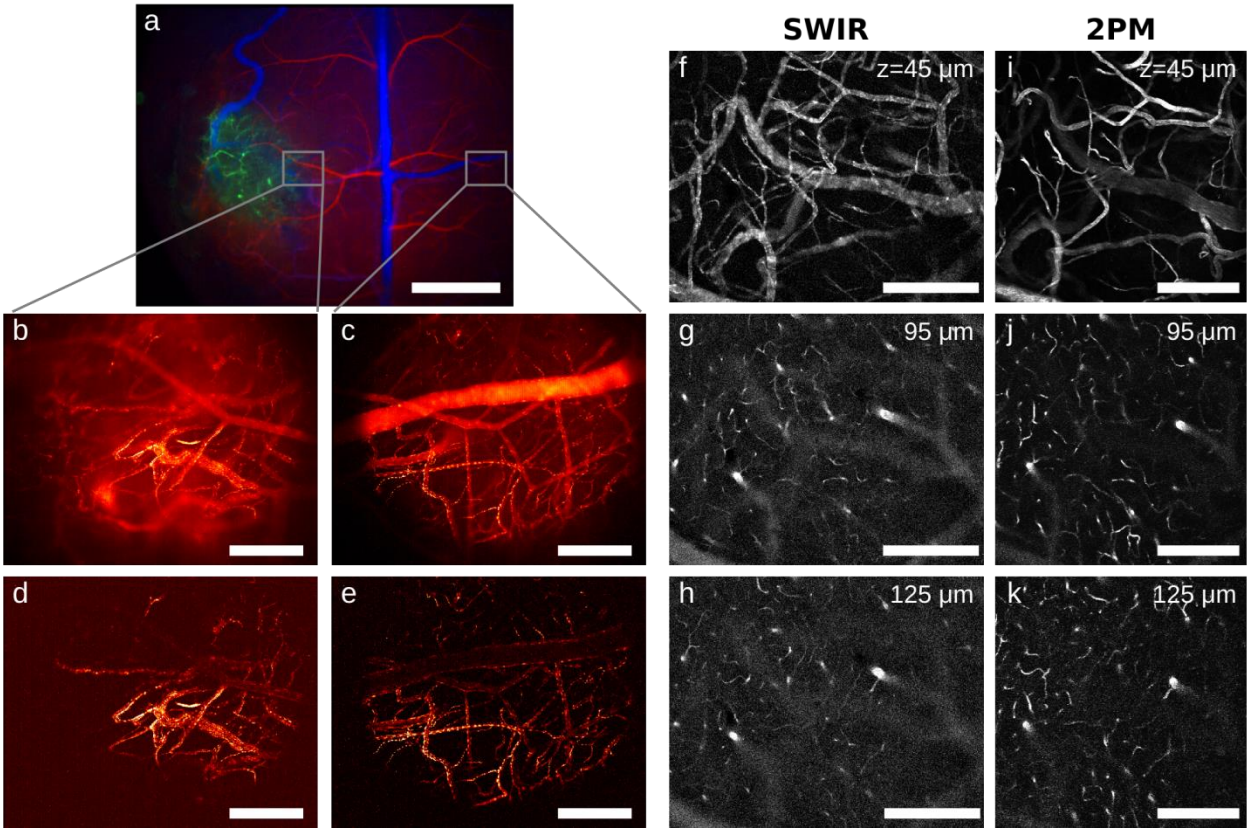


**Figure 6: High resolution high-speed QD-SWIR intravital imaging.**

In addition to generating a multicolor angiography image of a glioblastoma tumor in a cranial window model (a) high-resolution high-speed QD-SWIR imaging at 60 fps was used to image the vascular network of the tumor margin (b) and to compare it to the vasculature in the contralateral hemisphere (c). Maximum intensity projections of 600 frames over 10 seconds are shown here. By subtracting the average signal of these 600 frames from the maximum intensity projection the signal originating only from individual QD-SWIR composite particles in the focus was isolated. This allowed isolating blood flow from the focal plane of the tumor margin (d) and the vessels on the contralateral lateral side (e). To enhance the contrast of the focal plane and provide true z-sectioning capability, we calculated the sum of the magnitude of the difference of each frame from the average, which is sensitive only to fluctuations over time, i.e. the transit of individual composite particles. Figures f—k directly compare the micrographs of the same fields of view of a healthy mouse brain at various depths taken by our novel z-sectioning approach

(f—i) and conventional multiphoton microscopy (i—k). Scale bars in b—e are 300 μm, and in f—k are 200 μm. Scale bar for (a) is 1500 μm, scale bars for (b—e) are 300 μm and scale bars for (f—k) are 200 μm.

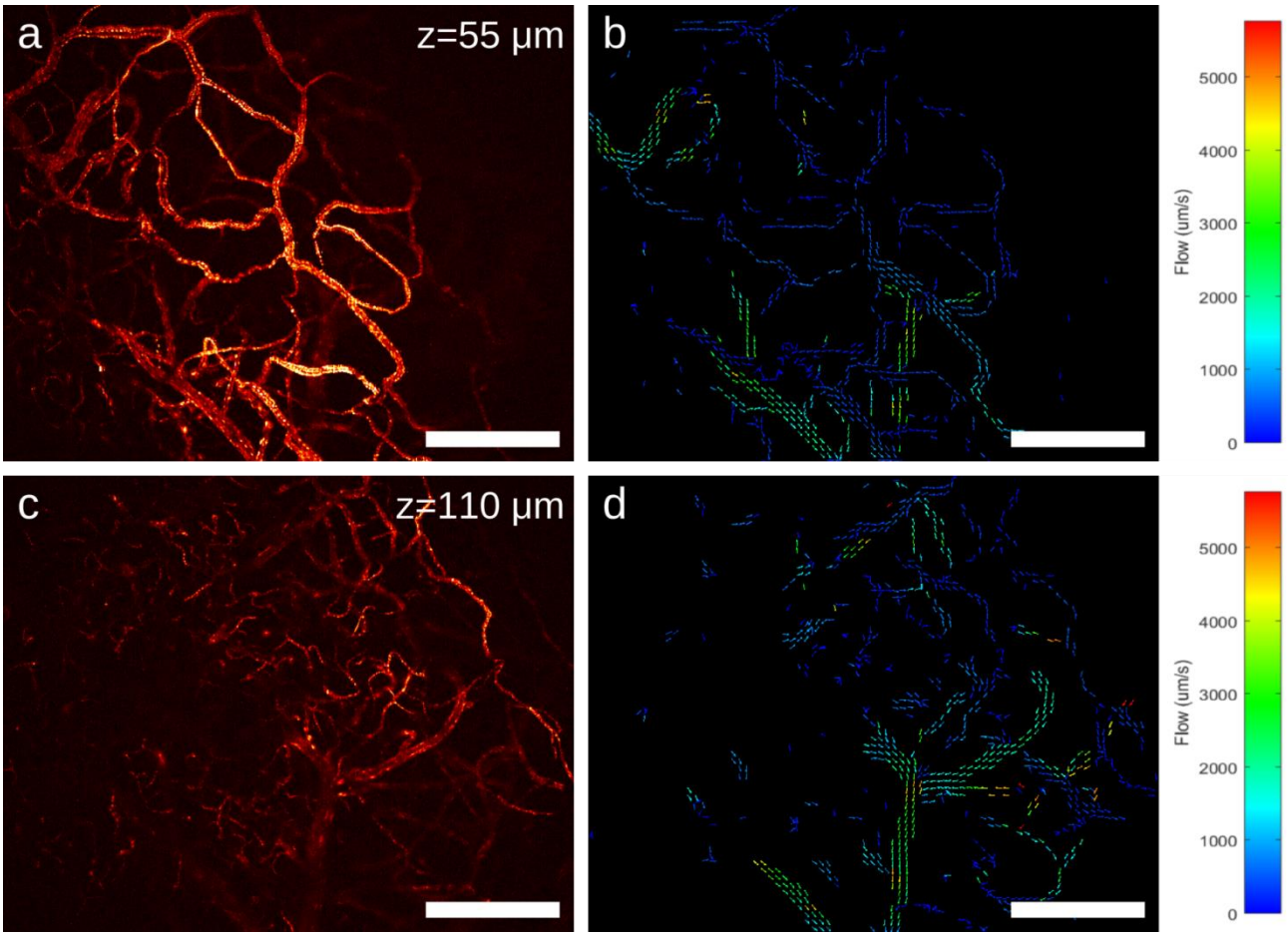


**Figure 7: High resolution high-speed QD-SWIR intravital imaging to generate flowmaps of microvascular networks.**

Applying our novel z-sectioning approach in 5 µm steps in a healthy mouse brain results in a z-resolved three-dimensional representation of the vascular network. Furthermore the signal from the particles in the focus (a and c; the difference from the average signal, maximum intensity projection of 600 frames), analyzed by a multi-pass particle image velocimetry (PIV) approach, generate a flow map for each slice (b and d, supplementary video 12). All scale bars are 300 µm, and the units for velocity are µm/s (b and d).